

Noise Modeling of Graphene Resonant Channel Transistors

Michael Lekas, Sunwoo Lee, Wujoon Cha, James Hone, *Member, IEEE*, and Kenneth Shepard, *Fellow, IEEE*

Abstract—In this paper, we present a compact model for graphene resonant channel transistors (G-RCTs) that uses extracted electrical and mechanical parameters to provide an accurate simulation of dc, RF, noise, and frequency-tuning characteristics of the device. The model is validated with measurements on fabricated G-RCTs, which include what we believe to be the first noise measurements conducted on any resonant transistor. The noise model, which considers both electrical and mechanical sources, is used to demonstrate the fundamental differences in the noise behavior of active and passive resonator technologies, and to show how optimization of device parameters can be used to improve the noise performance of RCTs.

Index Terms—Compact model, graphene, noise, resonant channel transistor (RCT), resonator.

I. INTRODUCTION

RESONANT channel transistors (RCTs) are active nanoelectromechanical devices in which the channel of a field-effect transistor (FET) is simultaneously used as a mechanical resonator and as a high-gain transducer of its own mechanical motion into an electrical signal. The active FET sensing used in RCTs contrasts with the capacitive or piezoelectric transduction used in passive resonator technologies, which trades increased parasitic capacitance and decreased out-of-band rejection for improved actuation and sensing [1].

RCTs belong to a family of resonant-transistor (RT) technologies, including resonant-body and resonant-gate devices, that break the trade-off between transduction and feedthrough parasitics. Due to this advantage, RTs are being explored for a range of potential applications in RF oscillator and filter circuits based on different material systems and using a variety of transduction modalities [2]–[7]. RCTs made from graphene are of particular interest because they take advantage of the

material's low mass (7.4×10^{-16} g/m²) and high stiffness (340-N/m in-plane Young's modulus) [8] to deliver resonant frequencies (ω_o) in the hundreds of megahertz at quality factors (Q) in excess of 100 at room temperature [9], and 10 000 at cryogenic temperatures [6]. High breaking strength (34 N/m) [10] allows graphene membranes to be fabricated in highly strained configurations, which further boost both Q and ω_o [11], [12], and graphene's high room temperature carrier mobility ($\mu > 10\,000$ cm²/V · s) results in an excellent signal transduction.

G-RCTs also have several advantages in fabrication over thin-film bulk acoustic resonators (FBARs) currently used in many RF applications. The first is that ω_o is a function of in-plane dimensions that are lithographically defined rather than layer thicknesses that characterize FBAR resonant frequencies. This makes it possible to create arrays of multifrequency devices on a single chip without a large number of deposition steps, facilitating the design of filter banks for applications, such as cognitive radio. Moreover, tuning of ω_o by more than 1 MHz/V using the gate-to-source dc bias voltage has been demonstrated [11], allowing G-RCT circuits to be dynamically tuned postfabrication. A final advantage is that high-quality CVD graphene can be easily grown in a separate process and transferred onto nearly any surface [13], facilitating integration of G-RCTs with a silicon-CMOS back-end metal stack.

To aid the design and optimization of circuits that use G-RCTs, an all-region compact model is required that not only models the ac and dc characteristics of the device, but also its intrinsic noise. Without a proper noise model, designers would be unable to simulate the noise figure (NF) of filter circuits or the phase noise of oscillator circuits based on G-RCTs. To the best of the authors' knowledge, no group has reported noise characterization results for any type of RT. Previous work on G-RCTs focused on modeling doubly clamped beam devices [14], and derived an expression for the drain current (I_d) of the device by superposing a large-signal model for a graphene FET (GFET) and a frequency-dependent small-signal model for an RCT. This approach is not conducive to circuit design because separate models must be used for ac and dc simulations, and since the ac model is formulated in terms of small-signal frequency-domain equations, it cannot be used in transient simulations that are necessary for observing start-up behavior in oscillators. Furthermore, physical behaviors such as variation of direct current–voltage (I – V) characteristics due to the changes in channel displacement, and any effects involving noise are entirely neglected by this model.

Manuscript received November 24, 2014; revised January 12, 2015 and February 9, 2015; accepted February 15, 2015. This work was supported in part by the Semiconductor Research Corporation, Durham, NC, USA, Nanoelectronics Research Initiative through the INDEX Center, in part by the Defense Advanced Research Projects Agency through the U.S. Office of Naval Research under Contract N00014-1210814, in part by the Air Force Office of Scientific Research, Arlington, VA, USA, under Grant FA9550-09-1-0705, and in part by the Qualcomm Innovation Fellowship. The review of this paper was arranged by Editor Z. Celik-Butler.

M. Lekas, S. Lee, and K. Shepard are with the Department of Electrical Engineering, Columbia University, New York, NY 10027 USA (e-mail: msl22@ee.columbia.edu; sl3229@columbia.edu; shepard@ee.columbia.edu).

W. Cha and J. Hone are with the Department of Mechanical Engineering, Columbia University, New York, NY 10027 USA (e-mail: wc2444@columbia.edu; jh2228@columbia.edu).

Color versions of one or more of the figures in this paper are available online at <http://ieeexplore.ieee.org>.

Digital Object Identifier 10.1109/TED.2015.2405540

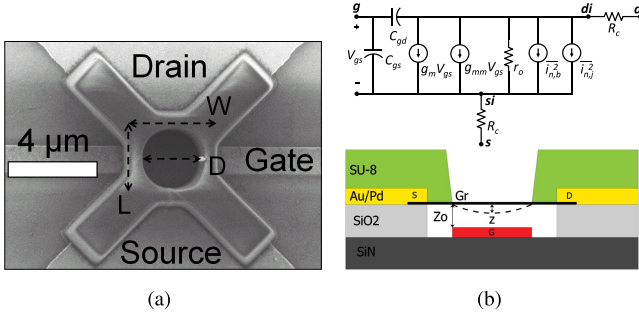


Fig. 1. (a) SEM image of a G-RCT. The channel width (W) and length (L) are the dimensions of the graphene strip. In our design, the SU-8 defines a suspended clamped drum region with a diameter D that is equal to L and slightly smaller than W . (b) Cross-sectional diagram and a small-signal model of a G-RCT. G , D , and S represent the gate, drain, and source electrodes, respectively. The source and drain electrodes have a 1-nm adhesion layer of titanium (not shown). The full metal stack for the electrodes is 1/15/50 nm of Ti/Pd/Au.

In this paper, we develop a more physical model for G-RCTs that enables simultaneous simulation of the dc, RF, and noise characteristics, as well as the electrostatic frequency tuning behavior of the device. The model is derived by coupling the analytical expressions for the charge in the graphene channel with the nonlinear time-varying (NLTV) equations that describe the resonator motion. This approach allows the circuit simulation environment (e.g., Agilent Advanced Design System (ADS) and Spectre) to directly solve for both the physical displacement of the resonator and I_d at each step in the simulation, creating a true physical link between the electrical and mechanical domains of operation. In addition, our study focuses on fully clamped circular drum resonators, which eliminate the spurious modes often seen in doubly clamped structures [11].

Section II describes the fabrication and operation of our G-RCTs. In Section III, we derive our compact model and validate it by comparing the simulation results with the measurements of fabricated devices. Section IV explains the formulation of a noise model for G-RCTs and verifies its accuracy with what we believe to be the first NF measurements on an RT. Finally, in Section V, an analytical expression for the NF of G-RCTs used as filtering elements is derived, and the trends predicted by the expression are verified through model simulations.

II. DEVICE FABRICATION AND OPERATION

Fig. 1(a) and (b) shows an SEM and a cross-sectional diagram of the G-RCT structure characterized in this paper, respectively. The device consists of a graphene sheet suspended above a metal gate by source and drain contacts made from palladium capped by gold. The graphene used in these devices is single layer, which is confirmed with the Raman spectra measurements of the graphene following CVD growth [10]. An SU-8 polymer clamp is lithographically patterned on top of the suspended graphene channel in a drum geometry. After SU-8 patterning, the devices are hard baked at 250 °C to crosslink the polymer, causing it to contract and apply additional strain to the graphene. A more detailed description of the device fabrication can be found in [11].

The suspended area of the channel is actuated by applying a dc bias $V_{gs,dc}$ and an RF signal amplitude of \tilde{V}_{gs} to the gate electrode. $V_{gs,dc}$ sets the polarity of the GFET structure and enables mechanical transduction. \tilde{V}_{gs} causes the channel to vibrate due to the electrostatic force, and the motion of the channel relative to the gate causes the capacitance of the structure to vary, modulating the channel charge density. Vibrations are sensed by applying a drain bias (V_{ds}) to the device and observing the resulting modulation in I_d .

Fig. 1(b) shows a small-signal circuit model for the device, including noise sources. The model is similar to that of a conventional FET, with the addition of an effective mechanical transconductance g_{mm} and a Brownian noise source $i_{n,b}^2$ (Section IV). The small-signal drain current is given by [15]

$$i_d = -j\omega C_{FT} \tilde{V}_{gs} - j\omega \frac{\tilde{z}}{z_0} C_{ge} V_{gs,dc} + g_m \tilde{V}_{gs} + g_m \frac{\tilde{z}}{z_0} V_{gs,dc} \quad (1)$$

where ω is the frequency of operation, \tilde{z} is the amplitude of vibration, z_0 is gate-to-channel spacing with $V_{gs,dc} = 0$, C_{ge} is the electrostatic gate-to-channel capacitance, g_m is the transconductance of the GFET, and C_{FT} is the total gate-to-drain capacitance including any parasitics. Due to the ambipolar nature of graphene, the sign of g_m can change depending on whether the device is biased for p- or n-type operation, and if V_{ds} is positive or negative. For the remainder of this section, we will assume the sign of g_m is positive.

The amplitude of vibration of the graphene membrane is given by

$$\tilde{z} = \frac{C_{ge} V_{gs,dc}}{m z_0} \left(\frac{1}{\omega_0^2 - \omega^2 + j\omega\omega_0/Q} \right) \tilde{V}_{gs} \quad (2)$$

where m is the resonator mass. The first two terms in (1) are the electrostatic and mechanical displacement currents seen in passive Microelectromechanical systems (MEMS) devices. The third term is identical to i_d for an FET, and the fourth term is the actively transduced mechanical signal. The third and fourth terms are typically an order of magnitude or more larger than the passive terms and dominate the frequency response. Using this approximation and inserting (2) into (1), a simplified expression for i_d can be written as

$$i_d(\omega) \simeq g_m \tilde{V}_{gs} + g_{mm} \tilde{V}_{gs} \quad (3)$$

$$g_{mm} = g_m \frac{C_{ge} V_{gs,dc}}{m z_0^2} \left(\frac{1}{\omega_0^2 - \omega^2 + \frac{j\omega\omega_0}{Q}} \right). \quad (4)$$

The first term in (3) is a background signal with a magnitude that is independent of ω , and a phase of 180°. The second term, representing the mechanical signal, is at its maximum near ω_0 , where it has a 90° phase shift due the quadrature relationship between the driving voltage and the motion of the channel at ω_0 ; away from ω_0 this term is small.

III. ELECTROMECHANICAL MODEL DESCRIPTION

To capture the full electromechanical behavior of the G-RCT and provide modeling across all regions of operation, we have developed a physics-based compact model implemented in Verilog-A, which includes both electrical and

kinematic components. The model combines a large-signal model for a GFET [16] with a continuum mechanics model for a 2-D membrane [17]. The basic operation of the model consists of the following steps.

- 1) The NLTV equations of motion for the mechanically resonant part of the channel are solved for its instantaneous displacement z based on applied terminal voltages.
- 2) The z -position is used to calculate the instantaneous value of the air-gap capacitance C_g in F/m².
- 3) C_g is applied to a GFET model to calculate the channel charge density and I_d .

The primary difference between our model and the model described in [14] is that we formulate the full equation of motion for the graphene channel such that the circuit simulator solves for z at each step, and the solution is directly used to solve for the channel charge. This model structure mathematically links the electrical and mechanical behavior of the device and leads to a more accurate representation of the physical system.

In our model, the quantum capacitance C_q of the graphene is neglected since the relatively large z_0 results in a smaller electrostatic capacitance that dominates the overall C_g . C_g is approximated as a parallel plate capacitance, which is divided into a dynamic component representing the suspended drum, and a static component representing the area under the SU-8 clamp, to properly model the motional and background currents in the device. The capacitance per unit area for the static region is given by

$$C_0 = \frac{\epsilon_0}{z_0} \quad (5)$$

where ϵ_0 is the vacuum permittivity. The dynamic region capacitance is given by

$$C_{g,\text{dyn}} = \frac{\epsilon_0}{z_0 - z}. \quad (6)$$

The NLTV equations of motion can be written in state-space form and implemented in Verilog-A as [18]

$$\begin{cases} \frac{dz}{dt} = v \\ \frac{dv}{dt} = \frac{1}{m}(F_e - F_s - F_d) \end{cases} \quad (7)$$

where v is the velocity of the resonator, F_e is the electrostatic force, F_s is the spring restoring force, and F_d is the damping force. The forces on the resonator are given by [17]–[19]

$$F_e = \frac{1}{2} V_{g,\text{ch}}^2 \frac{\epsilon_0 A_{\text{dyn}}}{(z_0 - z)^2} \quad (8)$$

$$F_s = \frac{8\pi E_{2-D}}{3(1 - \nu_p^2) R^2} z^3 + \frac{2\pi E_{2-D} \sigma}{1 - \nu_p^2} z \quad (9)$$

$$F_d = bv \quad (10)$$

where E_{2-D} is the in-plane Young's modulus of graphene, ν_p is Poisson's ratio, R is the drum radius, σ is the built-in strain of the membrane due to the SU-8 clamp, b is the damping coefficient, $A_{\text{dyn}} = \pi R^2$ is the area of the drum, and $V_{g,\text{ch}}$ is the channel actuation voltage, given by

$$V_{g,\text{ch}} = V_{gs} - \frac{1}{2} V_{ds} \quad (11)$$

where $V_{g,\text{ch}}$ is set equal to the potential between the gate and the midpoint of the channel, instead of the gate-to-source voltage V_{gs} , to account for the fact that the quiescent electrostatic force on the drum is not uniform across the channel length due to V_{ds} . The damping coefficient is calculated from the spring constant of the membrane k_s as

$$b = \frac{\sqrt{k_s m}}{Q} \quad (12)$$

$$k_s = \frac{8\pi E_{2-D}}{(1 - \nu_p^2) R^2} z^2 + \frac{2\pi E_{2-D} \sigma}{1 - \nu_p^2} - V_{g,\text{ch}}^2 \frac{\epsilon_0 A_{\text{dyn}}}{(z_0 - z)^3}. \quad (13)$$

In this formulation, F_s is given specifically for a 2-D circular membrane, but the spring force of a different geometry (e.g., doubly clamped beams) could be substituted to apply the model to a different type of RCT.

I_d for the GFET structure is given by [16]

$$I_d = \frac{q \mu W \int_0^{V_{ds}} n[V(x)] dV}{L - \mu \int_0^{V_{ds}} \frac{1}{v_{\text{sat}}} dV} \quad (14)$$

where q is the elementary charge, W is the channel width, μ is the effective mobility, and $n[V(x)]$ is the channel carrier concentration at a given position x along the channel associated with a local potential V . The denominator of (14) can be simplified by approximating the saturation velocity v_{sat} with an average value for the entire channel with

$$v_{\text{sat}} \approx \frac{\omega_{\text{ph}}}{\sqrt{\pi n_{\text{mid}}}} \quad (15)$$

where n_{mid} is the carrier density calculated at the midpoint in the channel written as

$$n_{\text{mid}} = \sqrt{n_0^2 + \left(\frac{C_0(V_{gs} - V_{gs0} - V_{ds}/2)}{q} \right)^2} \quad (16)$$

where V_{gs0} is the gate-to-source voltage at the Dirac point, n_0 is the minimum sheet carrier concentration at this voltage, and $\hbar\omega_{\text{ph}}$ is the dominant phonon energy. Since the device is not substrated, the zone-edge optical phonon of graphene (160 meV) is used [20]. We note that this is the appropriate value for suspended graphene, but may not be correct for the graphene in contact with the SU-8. We account for any error introduced by this value with a fitting parameter M shown later. Applying this approximation, v_{sat} can then be moved outside the integral.

The current contributions from the static and dynamic regions to I_d are computed separately since they are functions of C_0 and $C_{g,\text{dyn}}$, respectively. The following equations show the analytical solution of the integral of the carrier density in the numerator of (14) for the dynamic region only; the equations for the static region are identical except for the substitution of C_0 in place of $C_{g,\text{dyn}}$:

$$\begin{aligned} & \int_0^{V_{ds}} n_{\text{dyn}}[V(x)] dV \\ &= n_{d,\text{lim}} - n_{s,\text{lim}} = n_{\text{dyn},\text{ch}} \end{aligned} \quad (17)$$

$$n_{d,\text{lim}} = \frac{1}{2} \left[-n_d V_{\text{ch},d} + \frac{n_0^2 \ln \left(\frac{-C_{g,\text{dyn}} V_{\text{ch},d}}{q} + n_d \right)}{C_{g,\text{dyn}}/q} \right] \quad (18)$$

$$n_{s,\text{lim}} = \frac{1}{2} \left[-n_s V_{\text{ch},s} + \frac{n_0^2 \ln \left(\frac{-C_{g,\text{dyn}} V_{\text{ch},s}}{q} + n_s \right)}{C_{g,\text{dyn}}/q} \right] \quad (19)$$

$$n_d = \sqrt{n_0^2 + \left(\frac{C_{g,\text{dyn}} V_{\text{ch},d}}{q} \right)^2}$$

$$n_s = \sqrt{n_0^2 + \left(\frac{C_{g,\text{dyn}} V_{\text{ch},s}}{q} \right)^2} \quad (20)$$

$$V_{\text{ch},d} = V_{\text{gs}} - V_{\text{gs}0} - V_{\text{ds}}, \quad V_{\text{ch},s} = V_{\text{gs}} - V_{\text{gs}0}. \quad (21)$$

Using (17)–(21), the final expressions for I_d can be written as

$$W_{e,\text{dyn}} = MD, \quad W_{e,\text{stat}} = W - W_{e,\text{dyn}} \quad (22)$$

$$I_d = q\mu \left[\frac{W_{e,\text{stat}} n_{\text{stat},\text{ch}}}{L + \mu \frac{V_{\text{ds}}}{v_{\text{sat}}}} + \frac{W_{e,\text{dyn}} n_{\text{dyn},\text{ch}}}{L + \mu \frac{V_{\text{ds}}}{v_{\text{sat}}}} \right] \quad (23)$$

where $W_{e,\text{dyn}}$ and $W_{e,\text{stat}}$ are the effective channel width for the drum and the clamped area, respectively. M is a dimensionless modification factor that accounts for the overestimate of $I_{d,\text{dyn}}$ that occurs since the integral of the carrier concentration across the drum region is for a circular rather than rectangular section of the channel. M is typically ~ 0.25 for this geometry. Series resistances at the source and drain (R_c) are also added to the model in Verilog-A as the branches between the intrinsic device and the drain and source pads. The final contributions to the model are the intrinsic gate-to-source and gate-to-drain capacitances, given approximately by

$$C_{\text{gd}} = \frac{C_0 WL}{2}, \quad C_{\text{gs}} = C_0 WL. \quad (24)$$

To verify the model, measurements were conducted on devices in a vacuum probe station at $P_0 < 10^{-6}$ torr. S -parameter (SP) measurements were conducted using an Agilent N5230A network analyzer in a standard two-port configuration with bias tee on the gate and drain. The mass and σ of the graphene membrane were extracted from the frequency tuning behavior of S_{21} as a function of V_{gs} using the continuum mechanics model, and Q was extracted from the full-width at half-maximum of S_{21} with the background g_m signal subtracted. Electrical parameters μ and $V_{\text{gs}0}$ were extracted from I – V measurements, and n_0 and R_c were used as fitting parameters. The full set of parameters for the device modeled in this paper is shown in Table I. The mass is given as a multiple of the intrinsic mass of the graphene drum m_0 ; m is typically larger than m_0 due to residue from fabrication.

I – V measurements of the device are compared with the simulations of the model conducted in ADS in Fig. 2. Fig. 3 shows the measured and simulated S_{21} as a function of frequency and V_{gs} , demonstrating that the model also accurately reproduces the strain-frequency tuning behavior. Slices of the S_{21} simulation from Fig. 3 and the measurements for $V_{\text{gs}} = -4.0$ V and $V_{\text{ds}} = -0.4$ V are compared in Fig. 4. All the measurements agree well with the simulation, although there is some discrepancy near the Dirac point in the low-field I – V shown in Fig. 2(b). This stems from a combination of neglecting C_q in our calculation of the channel charge, and error in the velocity saturation model [16] that only

TABLE I
MODEL PARAMETERS

Parameter	Value
L	$2 \mu\text{m}$
W	$4 \mu\text{m}$
D	$2 \mu\text{m}$
z_0	115 nm
Q	39
m	$6.53 m_0$
σ	0.00077
μ	$3250 \text{ cm}^2/\text{V} \cdot \text{s}$
n_0	$3.72 \times 10^{11} \text{ cm}^{-2}$
R_c	$190 \Omega \cdot \mu\text{m}$
$V_{\text{gs}0}$	2.5 V
M	0.25

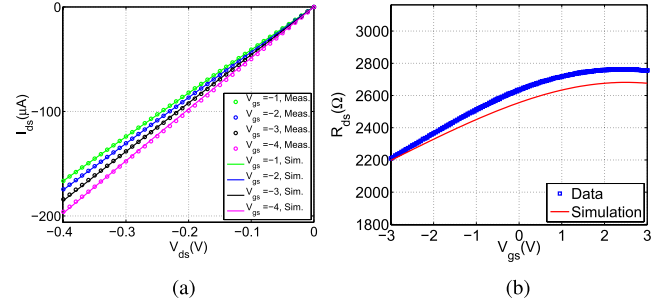


Fig. 2. (a) High-field I – V measurements and simulation. (b) Low-field I – V measurement and simulation at $V_{\text{ds}} = 10$ mV.

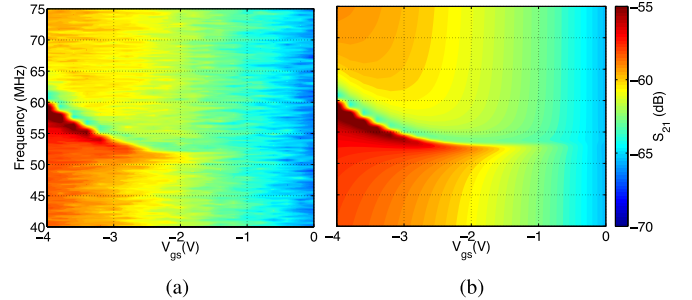


Fig. 3. (a) Measured and (b) simulated S_{21} as a function of frequency and V_{gs} . Both simulation and measurement were conducted at 21 V_{gs} points. The compact model replicates the strain-frequency tuning behavior of the graphene drum.

becomes noticeable at low charge densities. However, G-RCTs are often operated at higher densities, where these effects are of little consequence.

IV. NOISE MODELING

The primary intrinsic noise sources in an RCT are the Johnson noise due to the channel resistance $i_{n,j}^2$, and the transduced Brownian noise due to the mechanical vibrations $i_{n,b}^2$. These are modeled as noise current sources, as shown in Fig. 1. The same expression used for $i_{n,j}^2$ in FETs is used in our model

$$i_{n,j}^2 = 4k_b T g_{d0} \gamma \quad (25)$$

where g_{d0} is the channel conductance at $V_{\text{ds}} = 0$ V [21], and $\gamma \sim 1$ for our RCTs because they do not saturate due to

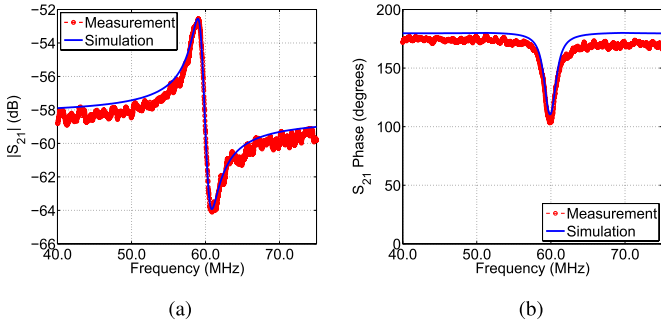


Fig. 4. Comparison of SP measurements and simulations for $V_{gs} = -4.0$ V and $V_{ds} = -0.4$ V. (a) Magnitude and (b) phase of the S_{21} . The phase of the device at resonance is $\sim 100^\circ$ rather than the 90° since g_m is still contributing a noticeable fraction of the output signal.

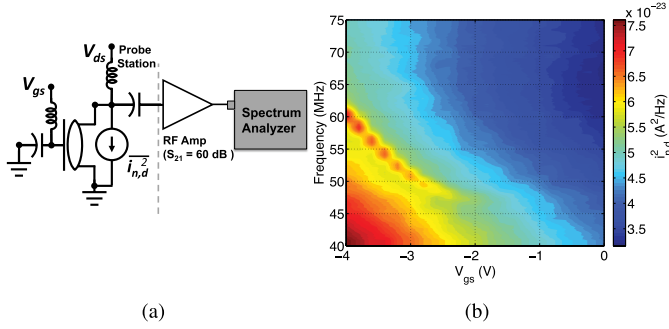


Fig. 5. (a) Noise measurement setup. The device is probed inside a vacuum probe station and an RF amplifier is placed on the RF port of a bias tee outside the probe station. (b) Measured drain current noise ($i_{n,d}^2$) as a function of frequency and V_{gs} for $V_{ds} = -0.4$ V. Both simulation and measurement were conducted at 21 V_{gs} points. The contribution of $1/f$ noise can be seen at lower frequencies.

their relatively large z_0 . $i_{n,b}^2$ is a function of the noise spectral density of vibrations z_n^2 (m^2/Hz) and the efficiency with which they are sensed. This is illustrated using the fourth term in (1) to write

$$i_{n,b}^2 = g_m^2 V_{g,dc}^2 \frac{z_n^2}{z_0^2} \quad (26)$$

where z_n^2 is given by [22]

$$z_n^2 = \frac{4k_b T \frac{\omega_0}{mQ}}{(\omega_0^2 - \omega^2)^2 + \left(\frac{\omega\omega_0}{Q}\right)^2}. \quad (27)$$

$i_{n,b}^2$ is included in the model by adding a force term F_b into (7) given by [18]

$$F_b = 4k_b T b. \quad (28)$$

The Johnson noise contributed by R_c is also included in the model.

To corroborate the model, measurements were performed using the setup shown in Fig. 5(a), which consists of a Miteq AU-1447 low-noise amplifier (LNA) and an Agilent E4440a spectrum analyzer. The measurements shown here were conducted in the dark; no difference was observed in the noise spectra when the device was measured with ambient illumination. Measurement system noise was removed from the data using the procedure described in [21]. Fig. 5(b) shows

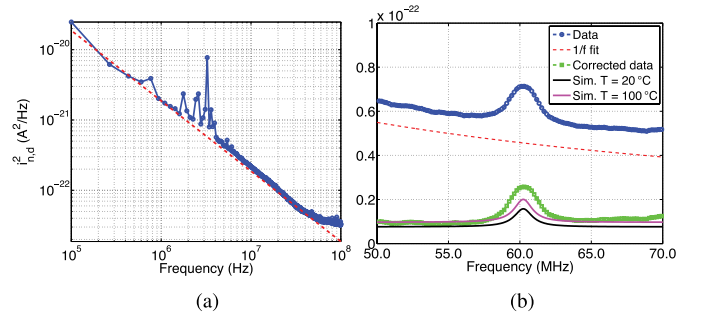


Fig. 6. (a) Large bandwidth noise measurement showing the $1/f$ spectrum and fit for $V_{gs} = 0$ V and $V_{ds} = -0.4$ V. Active sensing is turned off for this bias so no noise peak is visible. The peaks near 3 MHz are interference coupling in from the dc supplies. (b) Noise measurement near $\omega = \omega_0$. The blue trace shows the original measured data comprised of $1/f$ noise, $i_{n,j}^2$, and $i_{n,b}^2$. Fitting and subtracting the $1/f$ noise yields the green trace. Two noise simulations are shown for 20 °C and 100 °C demonstrating that the effect of heating is small. Simulations are shifted by 900 kHz to align them with the measured peak for illustration purposes.

the measured drain current noise $i_{n,d}^2$ as a function of V_{gs} and frequency. The peak in the noise spectrum of Fig. 5(b) has a similar tuning behavior to the S_{21} data shown in Fig. 3, but exhibits a slightly larger frequency range. The difference between the $i_{n,d}^2$ and S_{21} tuning may be due to the following.

- 1) Desorption of residue from the graphene between the time the noise and SP measurements were taken, resulting in decreased m and higher ω_0 .
- 2) Some slight nonlinear Duffing behavior occurring during the SP measurement that is altering the shape of the tuning characteristic.

In addition to $i_{n,b}^2$ and $i_{n,j}^2$, our G-RCT devices had a level of $1/f$ noise comparable with that measured in other graphene samples [23]–[25]. The device modeled in this paper had a noise amplitude $A \sim 7.8\text{e-}8$, where $A = (\omega/2\pi) i_{n,d}^2 / I_d^2$. However, due to the relatively low g_{d0} of the G-RCTs characterized for this paper and their resulting low Johnson noise floor, the $1/f$ corner frequency was often greater than 50 MHz. This is evident in Fig. 5(b) where the noise increases at lower frequencies, and makes it necessary to subtract the contribution of the $1/f$ noise to examine $i_{n,b}^2$ and $i_{n,j}^2$. Future devices should have lower channel resistances as the μ of the graphene improves, which will lower the corner frequency.

Fig. 6(a) shows a noise measurement between 100 kHz and 100 MHz on the same device modeled in the Section III, which is used to fit the $1/f$ noise. The resulting output noise spectrum after removing the $1/f$ noise is shown in Fig. 6(b). The corrected spectrum shows that away from ω_0 , a white noise floor due to $i_{n,j}^2$ dominates, and near ω_0 the contribution of $i_{n,b}^2$ rises and the noise spectrum peaks. We do not observe a change in the white noise floor of the device when the drain bias is removed, which suggests that the contribution of shot noise is negligible. Fig. 6(b) also shows the model simulations of the noise spectra for two different channel temperatures, since it is reasonable to assume some amount of heating for a nonsubstrated device with these dimensions [20].

The white noise background due to $i_{n,j}^2$ appears to be well modeled. The discrepancy between the values of the measured noise peak and the simulation is most likely due to

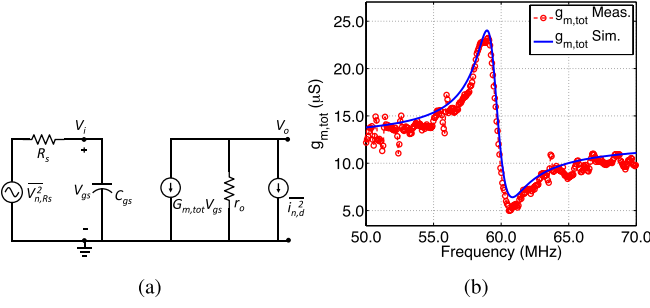


Fig. 7. (a) Simulated and measured total transconductance extracted from Y -parameters as a function of frequency for $V_{gs} = -4.0$ V and $V_{ds} = -0.4$ V. (b) Circuit schematic used for NF calculation.

an underestimate of the extracted Q resulting from the weak mechanical nonlinearity previously noted.

V. NOISE FIGURE PERFORMANCE OF G-RCT DEVICES

For RF filter applications, the primary figure of merit for describing the signal-to-noise performance of resonators is NF. For passive resonator technologies, such as FBARs and capacitive Si-MEMS, the NF of a resonator is equivalent to the power loss L between its input and the output ports [26]. $L = P_{in,av}/P_{out,av}$, where $P_{in,av}$ and $P_{out,av}$ are the power available from the source and the output of the device, respectively. This is because passive devices are typically reciprocal networks. RTs are also passive in the sense that they do not add power gain to a signal at their current reported performance levels [1], [3], [9], but the use of FET sensing makes them nonreciprocal such that L and NF are no longer equivalent. To highlight the ramifications of this nonreciprocity, an analytical expression for the NF of a G-RCT is derived in this section. The 50- Ω NF of the device characterized above is also calculated from the measurement of $i_{n,d}^2$ and compared with the simulations of NF and L .

In our analysis, we only consider the NF at $\omega = \omega_0$. In addition, we assume that ω is low enough that effects involving feedback through C_{gd} can be ignored, and the input impedance of the RCT is large relative to the source resistance R_s so that voltage noise due to R_s ($V_{n,Rs}^2$) is applied entirely across C_{gs} . We further assume that at $\omega = \omega_0$, the mechanical signal dominates and the first term in (3) can be neglected.

The noise factor F can be calculated as the ratio of the total output noise of the circuit shown in Fig. 7(a) to the output noise without the contribution of RCT noise sources, and is given by

$$F = 1 + \frac{i_{n,b}^2 + i_{n,j}^2}{V_{n,Rs}^2 g_{mm}^2} = 1 + \frac{g_m^2 V_{g,dc}^2 \frac{z_n^2}{z_0^2} + 4k_b T g d 0 \gamma}{4k_b T R_s g_{mm}^2}. \quad (29)$$

We neglect the contribution of $1/f$ noise in our calculation because, although it may be a large contributor to NF at low frequencies, we are primarily interested in the performance of the device as it scales to higher frequencies. $1/f$ noise is also neglected in the NF analysis of other RF components because its contribution to the noise spectra is typically far from the band of operation [26]. In addition, for $\omega = \omega_0$, (29) can be

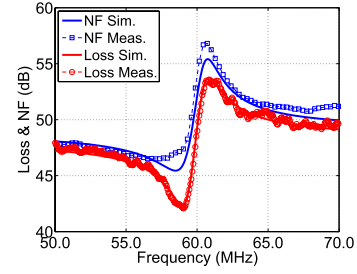


Fig. 8. Simulated and measured NF and L as a function of frequency for $V_{gs} = -4.0$ V and $V_{ds} = -0.4$ V. R_s was at 290 K and the device was at 100 °C in the simulation. NF is slightly higher than L near the resonance due to the additional contribution of $i_{n,b}^2$. The simulation gives a more optimistic value for NF due to the lower simulated $i_{n,b}^2$.

rewritten as

$$F = 1 + \frac{\sqrt{mk_s} z_0^4}{R_s V_{g,dc}^2 \epsilon_0^2 A^2 Q} + \frac{g d 0 \gamma z_0^6 k_s^2}{R_s g_m^2 V_{g,dc}^4 \epsilon_0^2 A^2 Q^2} \quad (30)$$

where A is the area of the actuator capacitance. The last term in (30), which is due to $i_{n,j}^2$, can be reduced by increasing g_m , as is commonly done in CMOS LNA designs. For G-RCTs, g_m may be increased by improving the μ of the graphene through cleaner growth and fabrication processes. The second term in (30) is due to $i_{n,b}^2$ and is not a function of g_m , so that as g_m increases L will continue to decrease, but NF will asymptotically approach a limit related to $i_{n,b}^2$. At this point, NF may only be further improved by enhancing actuation through the adjustment of mechanical parameters such as z_0 , Q , σ , and m .

F can be calculated from measurements as

$$F = 1 + \frac{i_{n,d}^2}{4k_b T R_s g_{m,tot}^2} \quad (31)$$

where $g_{m,tot} = y_{21} - y_{12}$ and represents the total device transconductance. L is calculated as the inverse of the available gain, given by [27]

$$L = \left(|S_{21}|^2 \frac{1}{1 - |S_{22}|^2} \right)^{-1}. \quad (32)$$

The NF calculations were performed with the $i_{n,d}^2$ spectrum shifted by 900 KHz relative to $g_{m,tot}$ to compensate for the aforementioned frequency shift between the SP and noise measurements. Fig. 7(b) shows the measured and simulated $g_{m,tot}$ as a function of frequency for $V_{gs} = -4.0$ V and $V_{ds} = -0.4$ V. We use this bias point for all the NF and L comparisons of Figs. 8–12. Fig. 8 shows the calculated and simulated NF and L as a function of frequency, demonstrating good agreement between the model and measurements. NF is several decibels higher than L , especially near ω_0 , where $i_{n,b}^2$ dominates. This verifies that the noise characteristics are in fact different from a reciprocal passive device. A NF higher than L occurs because the G-RCT introduces signal loss as well as active noise sources. The slight disagreement between the simulated and measured NF near ω_0 results from the underestimate of $i_{n,b}^2$ in the simulation shown in Fig. 6(b).

With this compact model, it is useful to investigate the effects of key design parameters on NF and L and validate

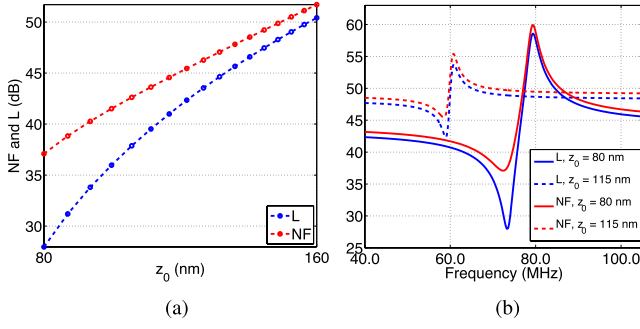


Fig. 9. (a) Simulated NF and L as a function of z_0 at resonance. (b) NF and L as a function of frequency for two values of z_0 , the parameter that has the largest influence on NF.

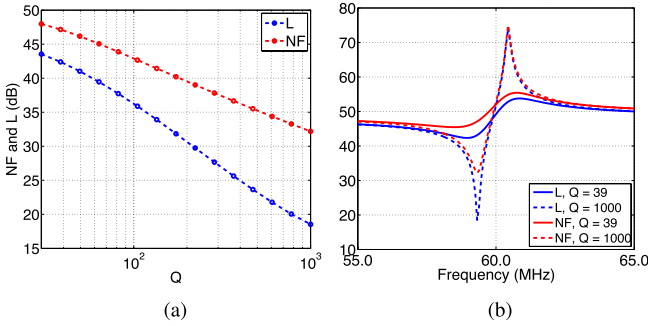


Fig. 10. (a) Simulated NF and L as a function of Q at resonance. (b) NF and L as a function of frequency for two values of Q .

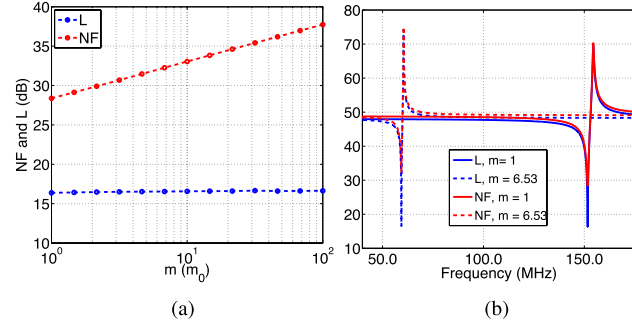


Fig. 11. (a) Simulated NF and L as a function of m at resonance. NF improves by 5 dB/decade of decrease in m , while L is unaffected. (b) NF and L as a function of frequency for two values of m . ω_0 increases by a factor of ~ 3 as m is lowered from its extracted value to m_0 . Q has been increased to 1000 in both plots.

the scaling trends predicted by (30). Fig. 9(a) shows the simulations of NF and L at $\omega = \omega_0$ as a function of z_0 using the parameters in Table I. NF improves at a rate of approximately 40 dB/decade of decrease in z_0 due to the z_0^4 in the second term of (30). Fig. 9(b) shows NF and L as a function of frequency for two values of z_0 , demonstrating that as z_0 is scaled down the rejection, given by the peak-to-background ratio of L , it improves from ~ 6 to ~ 13 dB. This behavior is very favorable for RF applications.

Fig. 10(a) shows NF and L at $\omega = \omega_0$ as a function of Q , and Fig. 10(b) shows NF and L as a function of frequency for two values of Q , both using the parameters in Table I. NF improves at a rate of approximately 10 dB/decade of increase in Q , which also indicates that the second term of (30) with Q in the denominator is dominant. Q can be improved in future G-RCTs by applying additional strain to the graphene

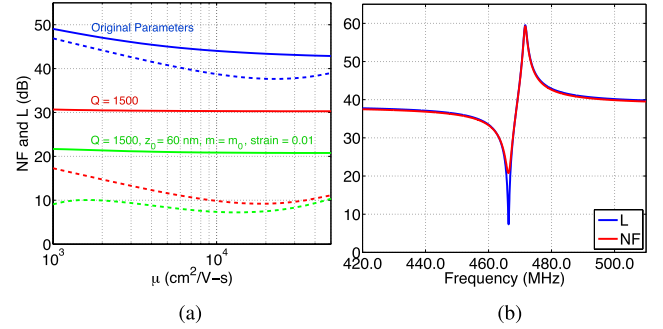


Fig. 12. (a) Simulated NF (solid) and L (dashed) as a function of μ at $\omega = \omega_0$ for the original parameters (blue), the original parameters with Q increased from to 1500 (red), and with the improved parameters of $z_0 = 60$ nm, $m = m_0$, $Q = 1500$, and $\sigma = 0.01$ (green). NF dependence on μ diminishes at higher values of Q . (b) NF and L as a function of frequency for $z_0 = 60$ nm, $m = m_0$, $Q = 1500$, $\mu = 10\,000$ $\text{cm}^2/\text{V-s}$, and $\sigma = 0.01$, showing that signal loss approaches 0 dB.

via the SU-8 clamp by hard baking the sample at a higher temperature [11], [12].

Fig. 11(a) shows NF and L at L at $\omega = \omega_0$ as a function of m , and Fig. 11(b) shows NF and L as a function of frequency for two values of m , respectively. In this simulation, the original extracted parameters are used with the exception of Q , which is increased to 1000. Again, the second term of (30) dominates and the \sqrt{m} in the numerator results in a 5 dB improvement in NF per decade of decrease in m . This effect is especially beneficial because it means that ω_0 can be scaled into the hundreds of megahertz and the NF of the structure can be improved simultaneously simply by improving the cleanliness of the graphene processing.

Fig. 12(a) shows how NF and L at $\omega = \omega_0$ are affected by changes in μ . The blue curves show the simulation results for the parameters in Table I, demonstrating that as the μ is increased NF initially improves commensurate with L , but eventually plateaus, due to the lack of a dependence on g_m in the second term of (30) previously mentioned. The red traces use the same parameters, except with Q increased to 1500. For these parameters, the dependence of NF on μ nearly vanishes, meaning that in this regime, improved FET sensing will boost signal gain, but will have little effect on noise performance. The green traces are for simulations with a variety of parameter improvements: $z_0 = 60$ nm, $m = m_0$, $Q = 1500$, and $\sigma = 0.01$. Fig. 12(b) shows NF and L as a function of frequency for the same improved parameters indicating that the combined scaling of z_0 , σ , and m boosts ω_0 into the UHF range, and drastically improves L and NF. We note that in Fig. 12(a), L does not decrease monotonically as μ increases due to the nonsaturating $I-V$ characteristics seen in these G-RCTs; as μ increases the device S_{21} increases, but the small-signal output resistance seen at the drain decreases, lowering the S_{22} and causing (32) to increase again at certain values of μ . This effect could be mitigated by further lowering z_0 to improve the electrostatic control of the gate on the channel.

Overall, our analysis of G-RCT noise has demonstrated that they may have worse NF performance than some passive resonator technologies due to their nonreciprocity and contributions of electrical and mechanical noise to I_d .

Although we have shown that the effect of device noise can be minimized through careful design, the level of performance seen in our simulations indicates that G-RCTs are not a good candidate for use in RF-front-end filters compared with state-of-the-art FBAR technology, which can achieve $NF < 5$ dB at multigigahertz frequencies.

Nonetheless, due to their advantages in terms of size, tunability, and the ease of integration of multifrequency arrays, they may still find application in RF filters that follow a LNA in a receiver, where NF is less critical. In this type of application, G-RCTs still have an advantage over passive MEMS devices, which suffer from the trade-off between rejection and transduction strength. As an example, one of the MEMS devices shown in [28] resonates at 1 GHz, but even when it is used in a circuit with a high terminating impedance (something that is difficult to achieve at these frequencies), the device still has a signal loss of greater than 20 dB, which is equivalent to its NF. In addition, G-RCTs are roughly an order of magnitude smaller than this device, and have far greater tunability.

Comparing G-RCTs with other types of RTs made from silicon or GaN, they all suffer from the added electrical and mechanical noise intrinsic to FET sensing of mechanical resonance. These devices also have similar Q s (~ 100), and mechanical or acoustic transconductances less than $50 \mu S$ [1], [3]. The G-RCT's primary advantage in relation to these technologies is its large frequency tuning range.

VI. CONCLUSION

In conclusion, we have developed a physics-based model for G-RCTs, which makes possible the simulation of hybrid electromechanical circuits, allowing, for example, cosimulation of G-RCTs with silicon CMOS technology. We verified that the model accurately replicates the dc, RF, and tuning characteristics of the device by comparing the simulation results with the measurements. In addition, we have measured the intrinsic noise of G-RCTs and have shown that our experimental results are in good agreement with our noise model.

To aid in the design of future devices, we have also derived an analytical expression for the NF of G-RCTs, and verified the scaling trends suggested by the expression through simulations of our compact model. Based on our observations, it should be possible, through careful parameter optimization, to fabricate low-noise G-RCTs operating in the hundreds of megahertz for signal processing applications. Moreover, the model proposed in this paper will aid the design of next generation G-RCTs and can be generalized for use with other types of RTs.

ACKNOWLEDGMENT

The authors would like to thank A. M. van der Zande, F. Lane, and V. Abramsky for their critical discussions.

REFERENCES

- [1] R. Marathe, B. Bahr, W. Wang, Z. Mahmood, L. Daniel, and D. Weinstein, "Resonant body transistors in IBM's 32 nm SOI CMOS technology," *J. Microelectromech. Syst.*, vol. 23, no. 3, pp. 636–650, Jun. 2014.
- [2] D. Weinstein and S. A. Bhavé, "The resonant body transistor," *Nano Lett.*, vol. 10, no. 4, pp. 1234–1237, 2010.
- [3] A. Ansari and M. Rais-Zadeh, "A thickness-mode AlGaIn/GaN resonant body high electron mobility transistor," *IEEE Trans. Electron Devices*, vol. 61, no. 4, pp. 1006–1013, Apr. 2014.
- [4] S. T. Bartsch, A. Rusu, and A. M. Ionescu, "Phase-locked loop based on nanoelectromechanical resonant-body field effect transistor," *Appl. Phys. Lett.*, vol. 101, no. 15, p. 153116, 2012.
- [5] C. Chen *et al.*, "Graphene mechanical oscillators with tunable frequency," *Nature Nanotechnol.*, vol. 8, no. 12, pp. 923–927, 2013.
- [6] C. Chen *et al.*, "Performance of monolayer graphene nanomechanical resonators with electrical readout," *Nature Nanotechnol.*, vol. 4, no. 12, pp. 861–867, 2009.
- [7] C.-H. Chin, C.-S. Li, M.-H. Li, and S.-S. Li, "A CMOS-MEMS resonant gate field effect transistor," in *Proc. 17th Int. Conf. Solid-State Sens., Actuators, Microsyst. (TRANSDUCERS EUROSENSORS XXVII)*, Jun. 2013, pp. 2284–2287.
- [8] C. Lee, X. Wei, J. W. Kysar, and J. Hone, "Measurement of the elastic properties and intrinsic strength of monolayer graphene," *Science*, vol. 321, no. 5887, pp. 385–388, 2008.
- [9] M. Lekas *et al.*, "Stress-enhanced chemical vapor deposited graphene NEMS RF resonators," in *Proc. Joint Eur. Freq. Time Forum Int. Freq. Control Symp. (EFTF/IFC)*, Jul. 2013, pp. 543–546.
- [10] G.-H. Lee *et al.*, "High-strength chemical-vapor-deposited graphene and grain boundaries," *Science*, vol. 340, no. 6136, pp. 1073–1076, 2013.
- [11] S. Lee *et al.*, "Electrically integrated SU-8 clamped graphene drum resonators for strain engineering," *Appl. Phys. Lett.*, vol. 102, no. 15, pp. 153101-1–153101-4, Apr. 2013.
- [12] Y. Oshidari *et al.*, "High quality factor graphene resonator fabrication using resist shrinkage-induced strain," *Appl. Phys. Exp.*, vol. 5, no. 11, p. 117201, 2012.
- [13] X. Li *et al.*, "Large-area synthesis of high-quality and uniform graphene films on copper foils," *Science*, vol. 324, no. 5932, pp. 1312–1314, 2009.
- [14] Y. Xu, O. Li, and R. Xu, "Graphene resonant channel transistor," in *Proc. IEEE Int. Wireless Symp. (IWS)*, Apr. 2013, pp. 1–6.
- [15] Y. Xu *et al.*, "Radio frequency electrical transduction of graphene mechanical resonators," *Appl. Phys. Lett.*, vol. 97, no. 24, p. 243111, 2010.
- [16] I. Meric, M. Y. Han, A. F. Young, B. Ozyilmaz, P. Kim, and K. L. Shepard, "Current saturation in zero-bandgap, top-gated graphene field-effect transistors," *Nature Nanotechnol.*, vol. 3, no. 11, pp. 654–659, 2008.
- [17] S. Timoshenko and S. Woinowsky-Krieger, *Theory of Plates and Shells*, vol. 2. New York, NY, USA: McGraw-Hill, 1959.
- [18] K. Van Caekenberghe, "Modeling RF MEMS devices," *IEEE Microw. Mag.*, vol. 13, no. 1, pp. 83–110, Jan./Feb. 2012.
- [19] L. D. Landau, *Theory of Elasticity*. Oxford, U.K.: Butterworth, 2008.
- [20] V. E. Dorgan, A. Behnam, H. J. Conley, K. I. Bolotin, and E. Pop, "High-field electrical and thermal transport in suspended graphene," *Nano Lett.*, vol. 13, no. 10, pp. 4581–4586, 2013.
- [21] A. A. Abidi, "High-frequency noise measurements on FET's with small dimensions," *IEEE Trans. Electron Devices*, vol. 33, no. 11, pp. 1801–1805, Nov. 1986.
- [22] J. S. Bunch *et al.*, "Electromechanical resonators from graphene sheets," *Science*, vol. 315, no. 5811, pp. 490–493, 2007.
- [23] Y. Zhang, E. E. Mendez, and X. Du, "Mobility-dependent low-frequency noise in graphene field-effect transistors," *ACS Nano*, vol. 5, no. 10, pp. 8124–8130, 2011.
- [24] Y.-M. Lin and P. Avouris, "Strong suppression of electrical noise in bilayer graphene nanodevices," *Nano Lett.*, vol. 8, no. 8, pp. 2119–2125, 2008.
- [25] G. Xu *et al.*, "Effect of spatial charge inhomogeneity on $1/f$ noise behavior in graphene," *Nano Lett.*, vol. 10, no. 9, pp. 3312–3317, 2010.
- [26] B. Razavi, *RF Microelectronics* (Prentice Hall Communications Engineering and Emerging Technologies), 2nd ed. Upper Saddle River, NJ, USA: Prentice-Hall, 2011.
- [27] G. Gonzalez, *Microwave Transistor Amplifiers: Analysis and Design*, vol. 2. Upper Saddle River, NJ, USA: Prentice-Hall, 1997.
- [28] L.-W. Hung and C. T. Nguyen, "Capacitive-piezoelectric transducers for high- Q micromechanical AlN resonators," *J. Microelectromech. Syst.*, doi: 10.1109/JMEMS.2014.2332991.